Journal of the European Ceramic Society 45 (2025) 117137

Contents lists available at ScienceDirect

Journal of the European Ceramic Society

journal homepage: www.elsevier.com/locate/jeurceramsoc

Direct Ink Writing of cobalt-zirconia monoliths for catalytic applications: A novel single-step fabrication approach

Seyed Ali Razavi [a,b], Gemma Fargas [a,b,*], Tània Vilella [b,c,d], Isabel Serrano [b,e], Miguel Ángel Laguna-Bercero [f], Luis Llanes [a,b], Daniel Rodríguez [b,c,d], Maria-Pau Ginebra [b,c,g,h], Jordi Llorca [b,e], Miguel Morales [a,b,*]

[a] CIEFMA-Department of Materials Science and Engineering, Universitat Politècnica de Catalunya, Barcelona-Tech, Campus Diagonal Besós-EEBE, Barcelona 08019, Spain
[b] Centre for Research in Multiscale Science and Engineering of Barcelona, Universitat Politècnica de Catalunya, Barcelona-Tech, Campus Diagonal Besós-EEBE, Barcelona 08019, Spain
[c] Biomaterials, Biomechanics and Tissue Engineering Group, Department of Materials Science and Engineering, Universitat Politècnica de Catalunya, Barcelona-Tech, Campus Diagonal Besós-EEBE, Barcelona 08019, Spain
[d] Institut de Recerca Sant Joan de Déu, Santa Rosa, 39-57, Esplugues de Llobregat, Barcelona 08950, Spain
[e] Institute of Energy Technologies and Department of Chemical Engineering, Universitat Politècnica de Catalunya, BarcelonaTech, Campus Diagonal Besós-EEBE, Barcelona 08019, Spain
[f] Instituto de Nanociencia y Materiales de Aragón, INMA, CSIC, Universidad de Zaragoza, Pedro Cerbuna 12, Zaragoza 50009, Spain
[g] Centro de Investigación Biomédica en Red-Bioingeniería, Biomedicina y Nanomedicina (CIBERBBN),Carlos III Health Institute, Madrid, Spain
[h] Institute for Bioengineering of Catalonia (IBEC), Barcelona Institute of Science and Technology, Barcelona, Spain

ARTICLE INFO

Keywords:
Additive manufacturing
Direct-Ink writing
Zirconia
Catalyst ethanol steam reforming
Hydrogen production

ABSTRACT

Additive manufacturing technologies are revolutionizing the fabrication of ceramic catalysts through hierarchical design to enhance catalytic performance and simultaneously improving the efficiency of the manufacturing process by decreasing the initial investment and production steps. This work proposes a fabrication process of cobalt-zirconia monoliths based on Direct-Ink Writing of Co-enriched hydrogel-based ceramic inks, and the debinding and sintering at 600ºC in a single thermal treatment. The effect of Co precursor amount (3.0 −7.0 wt% Co) on the rheological properties of inks and the catalytic performance in ethanol steam reforming is investigated. The results reveal the successful incorporation of Co into rectilinear monoliths with 50 % infill, obtaining strongly Co-rich surfaces. The remarkable catalytic performance of the 5.0 wt% Co monolith at 300–600ºC confirms the feasibility of this novel single-step approach, reaching an appropriate balance between catalytic activity and printability. This outcome may represent a push towards the fabrication of fully 3D-printed monolithic catalysts.

1. Introduction

Traditionally, the heterogeneous catalytic reactions are usually carried out in fixed-bed reactors using powder or pellet catalysts [1,2]. However, the fixed-bed reactors present some drawbacks, such as a low space rate, a high-pressure drop and the possibility of hot spot formation in exothermic reactions [3,4]. Alternatively, honeycomb-like structured reactors can be an interesting option to enhance the reaction efficiency, as these monoliths enable higher space rates compared to fixed-bed reactors, reducing pressure drop and diffusional resistance [3,5]. Honeycomb-like structured reactors typically consist of simple channel 3D-structures fabricated through extrusion and covered by a catalyst. Although these monolithic structures are widely implemented in the automotive sector for exhaust gas conversion and various other processes [6,7], they are strongly limited in shape and surface–to–volume ratio, which reduces the conversion of reactants [2]. In addition, the monolithic catalysts prepared by traditional methods like impregnation and wash-coating usually consist of three components: the monolithic structure support, a secondary layer, which acts as a binder, and the catalyst [1,8]. The monolithic structure, usually made of an inexpensive

* Corresponding authors at: CIEFMA-Department of Materials Science and Engineering, Universitat Politècnica de Catalunya, Barcelona-Tech, Campus Diagonal Besós-EEBE, Barcelona 08019, Spain.
E-mail addresses: gemma.fargas@upc.edu (G. Fargas), miguel.morales-comas@upc.edu (M. Morales).

https://doi.org/10.1016/j.jeurceramsoc.2024.117137
Received 2 November 2024; Received in revised form 30 November 2024; Accepted 5 December 2024
Available online 6 December 2024

Table 1
The component composition of the different inks.

Sample	Cobalt (wt%)	Cobalt (II) acetate tetrahydrate (wt%)	YDZ (wt %)	Solid loading (wt %)	Hydrogel (wt%)
YDZ	0	0	70.0	70.0	30.0
3Co-YDZ	3.0	12.7	57.3	70.0	30.0
5Co-YDZ	5.0	21.1	48.9	70.0	30.0
7Co-YDZ	7.0	29.6	40.4	70.0	30.0

ceramic material like alumina, cordierite, or mullite, presents a large density of channels and inner porosity. These characteristics provide good mass transfer, heat transfer, thermal and mechanical properties and also low-pressure drop. The secondary layer has often a large specific surface area to disperse the catalytic active species. The catalytic active species are deposited on the secondary layer usually by impregnation and calcination of the corresponding precursors. Monoliths are coated with the secondary layer typically by dip-coating [9–11], impregnation [12,13] or infiltration [14]. These methods are simple but usually require repeated cycles of coating or immersion and drying to obtain a desired loading. This reduces reproducibility, is time-consuming, and implies multiple thermal treatments are applied to each functional ceramic layer [15]. Thus, the future progress in catalytic reactors is clearly limited by the conventional manufacturing routes.

In recent years, additive manufacturing (AM) technologies have experienced a significant advance in solving drawbacks associated with limitations in the traditional fabrication methods of monolithic catalysts [16–19]. In particular, Direct Ink Writing (DIW), also known as robocasting and extrusion-based additive manufacturing (EAM), enables to overcome the limitations of fixed-bed and honeycomb-like structured reactors by tailoring geometrical features such as channel geometry, diameter, shape, porosity, and surface–to–volume ratio, for the targeted requirements [20–22]. In this regard, it is possible to maximize mass and heat transfer, leading to more active and stable catalytic reactors [21], decreasing energy consumption, and increasing the product efficiency. However, most of the reported approaches still require several post-treatments for their functionalization such as impregnation and washcoating, which, again, needs multiple thermal treatments applied to each functional ceramic layer [8,23–25].

Regarding ceramic materials for catalytic applications, the most widely used oxides are Al_2O_3, CeO_2, SiO_2, ZrO_2, and TiO_2, as well as more or less complex combinations of some of these containing the presence of doping agents in low proportion. There are also aluminosilicates such as clays or zeolites and SiC. Among them, yttria-doped zirconia (YDZ) has received particular interest due to its excellent mechanical properties, high temperature and thermal shock resistance, low thermal conductivity, and chemical stability. For energy and environmental applications, doped zirconia has also been used as a support for metallic nanoparticles in heterogeneous catalysis [26] such as Ru/yttria-stabilized zirconia (YDZ) for CO_2 hydrogenation [27]; Ru-$Ce_{0.7}Zr_{0.3}O_{2-\delta}$ for the partial oxidation of dimethyl ether [28]; Pt/YDZ for the oxidation of ethylene [29], toluene [30] and carbon monoxide [31,32]; Rh, Pt, and Pt-Rh/ZrO_2 for the clean-up of gasification gas [33,34]; and porous YDZ membranes [35] and Pt/YDZ [36,37] for Diesel soot oxidation, as well as YDZ electrolytes for Solid Oxide Fuel Cells (SOFCs) and Electrolysers (SOECs) [38,39], among others.

Following the above ideas, this work aims to fabricate Co-YDZ monoliths through DIW and sintering process to carry out the ethanol steam reforming. The latter is used as a reaction test for this proof-of-concept study. Co and YDZ have been selected as metallic active and ceramic support phases, respectively. Co is a relatively cheap non-noble metal with proven catalytic activity in the steam reforming of ethanol [40–46]. Meanwhile, YDZ is an active support for this reaction and, as a support, provides metal dispersion and enhances stability against coarsening during calcination and operation processes [35]. This novel approach is based on 3D co-printing and co-sintering of Co and YDZ precursors of catalysts to mimic Co-YDZ coated ceramic monoliths [25]. It holds the potential to significantly reduce both costs and time in the global production steps of monolithic catalysts. For this purpose, Co-enriched and water-based YDZ ceramic inks with loadings of 3.0–7.0 wt% Co are prepared. In doing so, three different percentages of cobalt (II) acetate tetrahydrate (3.0, 5.0 and 7.0 wt%) are added to the YDZ ceramic paste prepared by mixing the hydrogel-based Pluronic® F-127. Rectilinear monoliths are printed at 50 % infill and sintered at 600°C in a single thermal treatment to obtain good catalytic activity. The effect of Co precursor on the rheological properties of the inks and the catalytic performance in the ethanol steam reforming reaction is explored. In addition, the chemical and microstructural properties of the catalyst, as well as the effectiveness of the incorporation of the metallic active phase into monolith structures, are studied. In doing so, advanced characterization techniques such as field emission scanning electron microscope (FE-SEM), high-resolution transmission electron microscopy (HR-TEM), X-ray photoelectron spectroscopy (XPS), and Raman spectroscopy are implemented.

2. Experimental procedure

2.1. Materials

Partially stabilized zirconia powder containing 3 mol% yttria (Tosoh, Japan), commercially called TZ-3YB-E and referred to as YDZ in this work, was chosen as the precursor material for the fabrication of the monoliths. According to Tosoh's datasheet, the density of this material sintered at 1450°C is 6.05 $g{\cdot}cm^{-3}$. Pluronic® F-127 (Sigma-Aldrich, USA) was also utilized as the binder for preparing the hydrogel to formulate the ink. The precursor agent for adding cobalt to the monoliths' surface was cobalt(II) acetate tetrahydrate (VWR, Spain).

2.2. Manufacturing methods

2.2.1. Ceramic ink preparation

Before manufacturing the monoliths using the DIW technique, the ink formulation was made of YDZ, cobalt(II) acetate tetrahydrate, Pluronic F-127, and distilled water. For this purpose, a hydrogel composed of 32 wt% Pluronic and 68 wt% distilled water was prepared using a dual asymmetric centrifugal mixer (Speed Mixer, DAC 150.1 FVZ-k) for 10 min. Subsequently, the prepared gel was cooled down at 4°C for 24 h. At this temperature, hydrogel in liquid form is suitable for ink preparation and the air bubbles escapes, due to the thermo-sensitive mechanical behavior of hydrogel [47]. Afterwards, the YDZ and cobalt acetate precursors in different percentages were added to the hydrogel for the ink preparation, also using the dual asymmetric centrifugal mixer at 3500 r.p.m. In all inks, the solid loading percentage was kept at 70 wt %. The ink composition was defined as the metallic cobalt percentage: 0, 3.0, 5.0, and 7.0 wt% Co, which were named as YDZ, 3Co-YDZ, 5Co-YDZ and 7Co-YDZ, respectively. Table 1 shows the component composition of the prepared inks.

2.2.2. Fabrication of monoliths

The DIW process was conducted using an extrusion-based 3D printer prototype manufactured by CIM-UPC (Spain). Initially, the monolith geometry was designed using Solidworks software. Subsequently, the Slic3r version 1.3.0 software was employed to generate a layer-by-layer model uploaded to the 3D printer machine. The prepared ink was charged into a 10 cm^3 polymeric syringe equipped with a Nordson-EFD nozzle featuring a minimum internal diameter of approximately 580 μm and set up in the printer. Monoliths with a rectilinear structure and 50 % infill were then printed on polymeric support at a printing speed of 4 $mm{\cdot}s^{-1}$. As shown in the CAD model of printed monoliths in Fig. 1, the

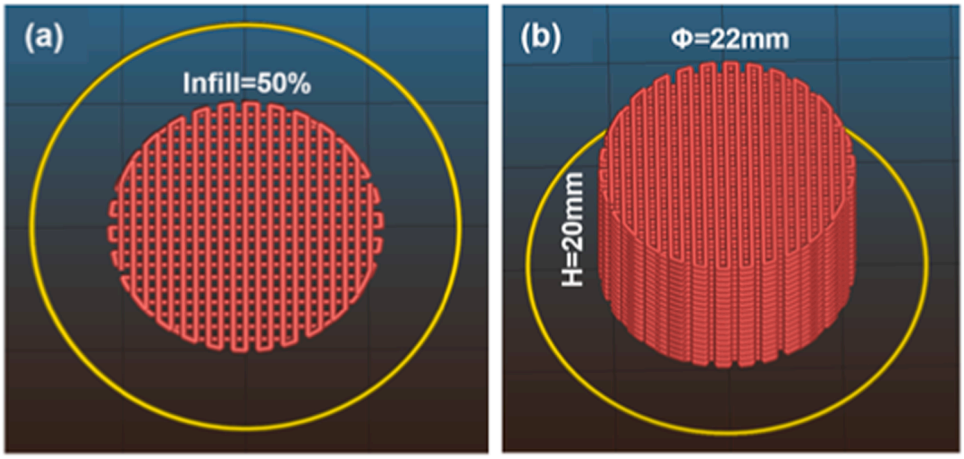

Fig. 1. Rectilinear monolith's CAD model, **(a)** top view, and **(b)** perspective view.

diameter and height of the printed sample were 22 mm and 20 mm, respectively. After printing the monoliths, they were dried under controlled conditions to reduce the formation of defects, such as cracks or delamination, due to the shrinkage produced during the drying process. The green body monoliths were introduced in a sealed box at 95 % relative humidity for 48 h. Subsequently, they were kept in a desiccator at a humidity of 75 % for 48 h, and finally kept at room conditions for at least 24 h.

After drying, a single thermal treatment was performed on green monoliths using a CARBOLITE Gero furnace (Germany) under an air atmosphere. The required thermal processing of 3D printed green ceramic parts involves two main steps to achieve the final functional device: (1) the organic burn-out process (so-called debinding), and (2) the coalescence of the ceramic particles during the sintering process. The specific parameters of the thermal treatment were selected according to previous works of the different materials present in the 3D printed monolithic catalyst.

2.3. Characterization methods

2.3.1. Characterization of precursor powders

Morphological characterization of the precursor powders was conducted using a field emission scanning electron microscope (FE-SEM, Carl Zeiss Merlin, Germany) equipped with Energy Dispersive Spectroscopy (EDS) (Oxford Instruments INCA-350 system, Germany). The particle size distribution of the powders was determined from the multiple FE-SEM images collected using the standard ISO 13322–1 [51], and the particle diameter measurements were conducted using ImageJ software [52].

2.3.2. Rheological characterization of inks

The rheological properties of the hydrogel as a gelling agent and prepared ink with different compositions were studied with a Discovery HR-2 rotational rheometer (TA Instrument). The rough parallel plates with 20 mm diameter were used for this test. Also, a 0.5 mm gap was considered between plates during the rheological test. The prepared inks were subjected to the flow sweep, amplitude sweep, and oscillatory 3-interval thixotropy test (3ITT) to evaluate their printability. These tests were selected based on the protocol introduced by del-Mazo-Barbara et al. [53,54]. The flow sweep test was conducted across shear rates ranging from 10 up to 200 s^{-1} to analyze the shear-thinning behavior. The selected shear rate range for the flow sweep test was specifically designed to align with the technical parameters of the printing process, ensuring the relevance and applicability of the results to the conditions used in this work. The Ostwald-de Waele power law was used to describe the flow behavior of viscous inks by calculating the relation between shear stress and shear rate:

$$\tau = k(\dot{\gamma})^n \tag{1}$$

In this equation, $\dot{\gamma}$ represents the shear rate, k is the flow consistency parameter, and n indicates the flow behavior index. Additionally, according to Eq. (2), the viscosity (η) is affected by the shear rate.

$$\eta = k(\dot{\gamma})^{n-1} \tag{2}$$

The value of n falling between 0 and 1 indicates pseudoplastic or shear-thinning behavior in the fluid. Additionally, the flow consistency parameter (k) exhibits a directly correlates with viscosity. Specifically, at a shear rate of 1 s^{-1}, the k equals the η in the fluid. The amplitude sweep test was utilized to determine the viscoelastic parameters of the inks. In this test, the frequency was maintained constant and equal to 1 Hz, and oscillations were conducted within the range of 100–5000 Pa. Storage modulus (G'), and loss modulus (G'') were simultaneously determined, along with yield stresses, where G' equals G''. This approach elucidated the distinct behavior of the inks based on the stress applied to them. For shape retention behavior simulated during a DIW process, an oscillatory 3-interval thixotropy test (3ITT) was conducted at 1 Hz frequency. The test has three sequential intervals with constant oscillatory strains. It starts with a low deformation stage (0.05 %) for 120 s, akin to the initial flow step in a printing syringe. Then, a high shear strain (400 %) is applied for 60 s to mimic ink extrusion through a small nozzle. Finally, another low-deformation stage (0.05 %) for 60 s represents the moment immediately after the ink is deposited on the platform.

2.3.3. Microstructural characterization of monoliths

Before characterization of the monoliths, the cross-section of coated filaments for the studied samples was prepared by grinding with 600-, 800-, and 1200-grit SiC papers, followed by subsequently polishing with 6 and 3 μm diamond suspensions (Norton, USA). The microstructural characterization of the samples was conducted using FE-SEM equipped with EDS. Cross-sections of the catalyst-layer microstructure were prepared using Focused Ion Beam (FIB, Carl Zeiss Neon 40, Germany). In order to prevent electrical charge of surface, the FE-SEM samples were coated with carbon. The determination and distribution of the phases in the monoliths were analyzed using FE-SEM, micro-Raman spectroscopy (inVia Qontor, Renishaw, United Kingdom), and X-ray diffraction (XRD, Bruker, D8-Advance, MA, USA). Raman measurements were conducted at room temperature, with a laser excitation wavelength of 785 nm. The samples were positioned for laser beam focusing using a 50x objective lens. Raman analysis was performed at various points across the cross-section of the filaments, at different depths relative to the filament surface. XRD analysis was carried out at ambient temperature using a Cu

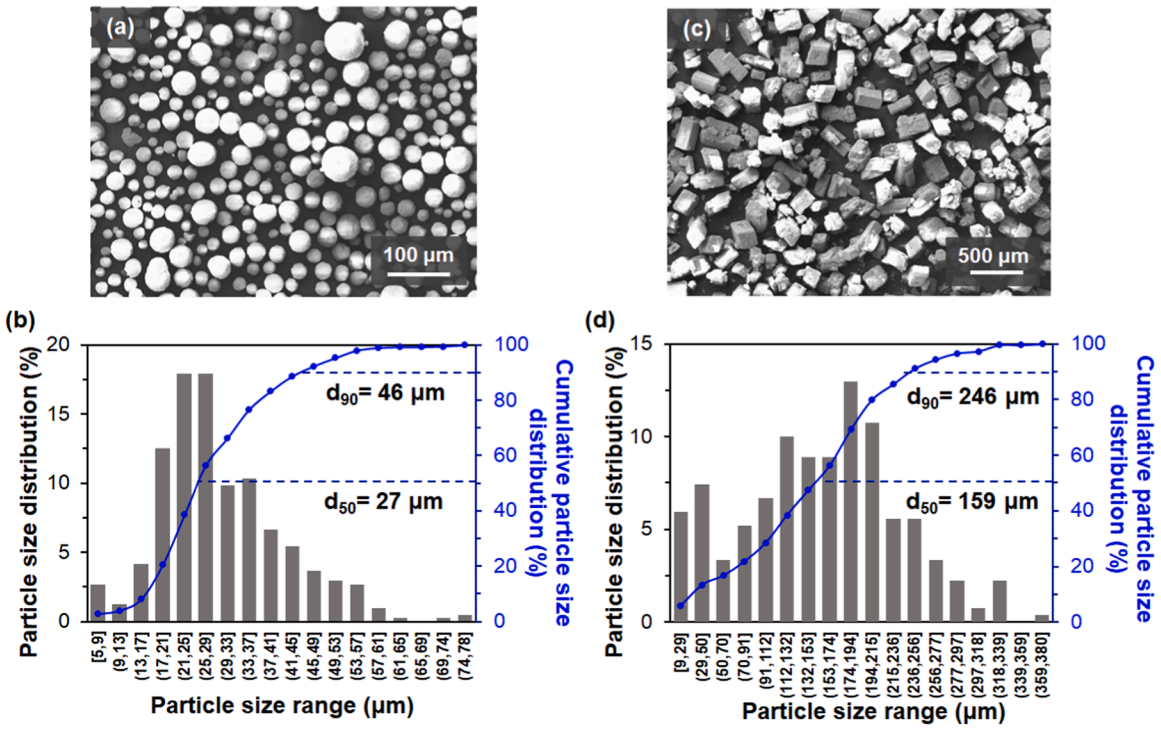

Fig. 2. SEM images and particle size distribution plots for the powders of: (a–b) YDZ and (c–d) cobalt acetate tetrahydrate.

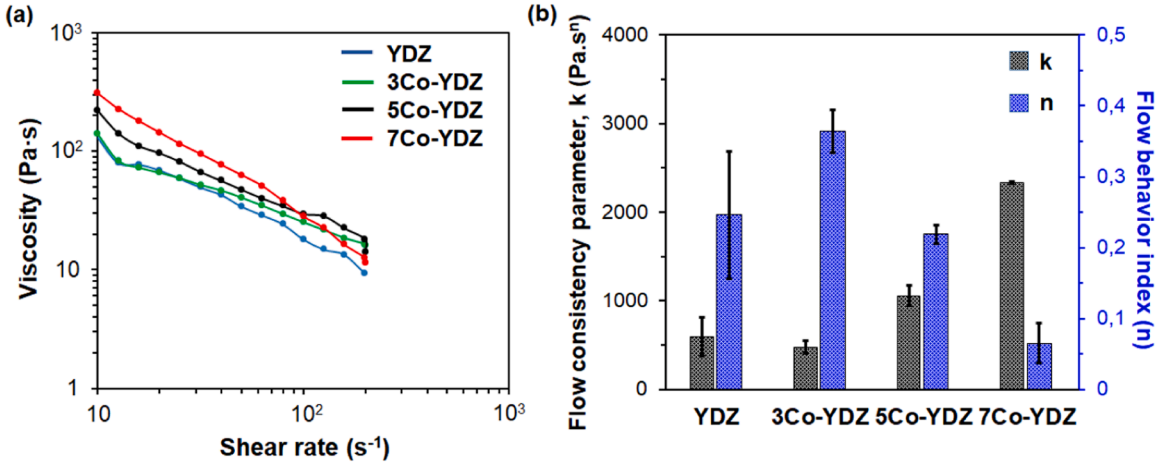

Fig. 3. (a) Effect of shear rate on viscosity, and (b) flow consistency parameter(k) and flow behavior index (*n*), for the prepared inks with different Co-YDZ formulations.

Kα radiation source (40 kV, 40 mA). Data were collected over a 2θ range of 20° to 80° with a step size of 0.01° and a scan rate of 1 s·step^{-1}. Phase identification was performed by comparing the XRD patterns to the Joint Committee on Powder Diffraction Standards (JCPDS) database using DIFFRACplus EVA software (Bruker AXS). The cross-section diameter and height of sintered samples were measured using a caliper. After the calculation of the monolith's volume, the shrinkage percentage (*S*) was calculated according to:

$$S(\%) = \frac{(V_0 - V_f)}{V_0} \times 100 \quad (3)$$

where the original and sintered monolith volumes, denoted by V_0 and V_f, were calculated from the SolidWorks model dimensions and the sintered monolith size. The chemical composition at the surface was determined by X-ray photoelectron spectroscopy (XPS) with a SPECS system (Surface Nano Analysis GmbH, Germany) equipped with an Al anode XR50 source operating at 150 W and a PHOIBOS 150 EP hemispherical energy analyzer with MCD-9 detector. The fitting and peak integration of spectra was carried out using Casa XPS software. The binding energies were calibrated to the C 1 s peak (284.6 eV) to compensate any charging effects. The general morphology of the catalyst and local chemical as well as structural information were studied by high resolution transmission electron microscopy (HR-TEM, Titan G2 60–300, USA), scanning transmission electron microscopy (STEM) imaging, and EDS analysis of the particles using a FEI Tecnai F30 operated at 300 kV.

2.3.4. Catalytic tests

The experiments were carried out in gas phase at atmospheric pressure under dynamic conditions. The experimental setup consisted of an argon stream bubbled through a saturator containing a mixture of water and ethanol. The resulting gaseous mixture of water:ethanol

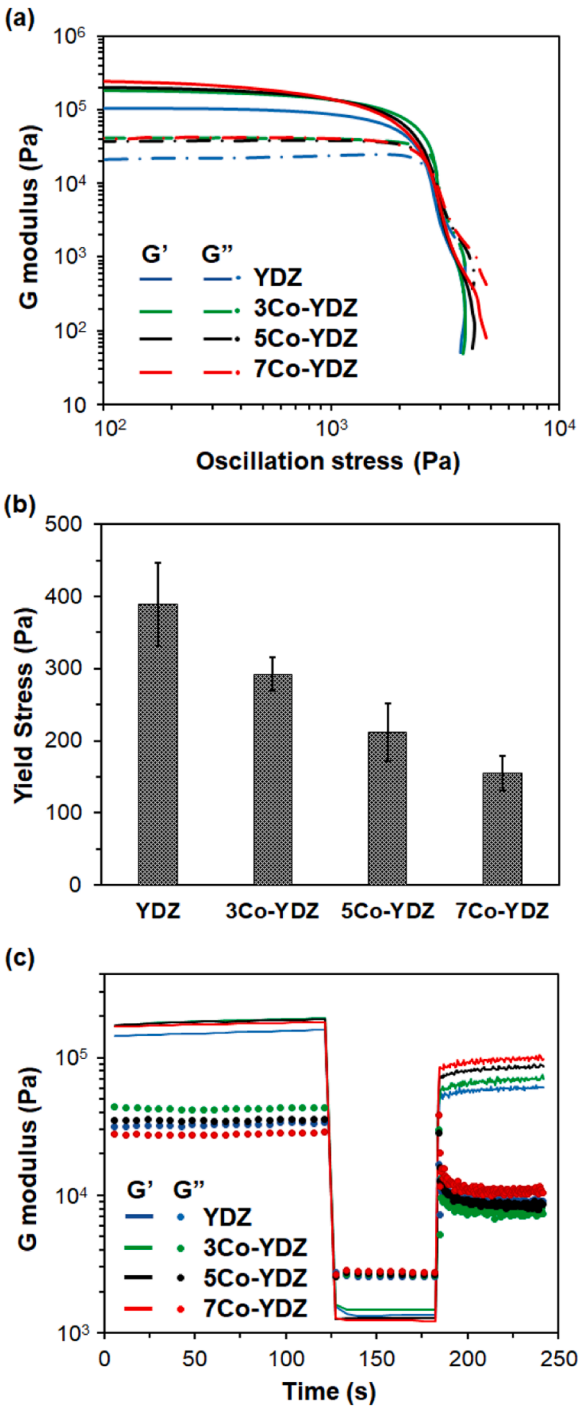

Fig. 4. (a) Evolution of oscillation stress effect on storage modulus (G') and loss modulus (G''), (b) related yield stress, and (c) inks shape retention capacity quantified through a 3-interval thixotropy test (3ITT), for the prepared inks with different Co-YDZ formulations.

(90:10, molar basis) was connected directly to the reactor, which was introduced in a furnace (± 0.1°C). The effluent was monitored online every 4 min with a micro-gas chromatograph (Agilent 490, USA). The experiments were carried out with an interval of temperatures ranging from 200 to 600°C, measuring the output gas composition every 50°C after stabilization. The gas hourly space velocity (GHSV) was determined at a constant flow rate of 20 mL·min^{-1} with respect to the monolith free volume, as follows:

$$\text{GSHV} = \text{volumetric gas flow rate/monolith free volume} \quad (4)$$

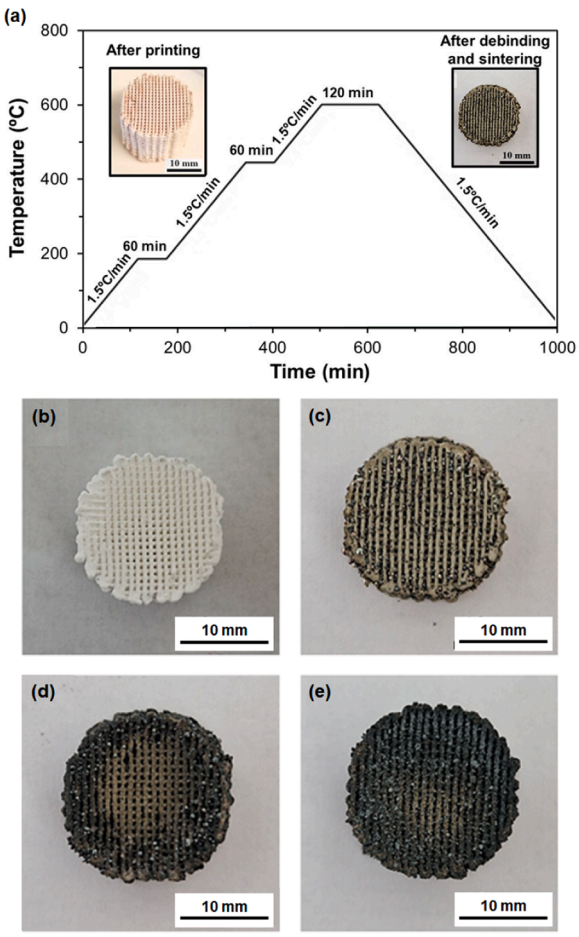

Fig. 5. (a) Thermal treatment of 3D printed monoliths and appearance of monoliths after sintering at 600°C for: (b) YDZ, (c) 3Co-YDZ, (d) 5Co-YDZ, and (e) 7Co-YDZ.

Gas residence time was determined as the inverse of the GHSV. The equations to determine the ethanol conversion and H_2 yield were as follows:

$$C_2H_6O\ conversion(\%) = \frac{n(C_2H_6O)_{in} - n(C_2H_6O)_{out}}{n(C_2H_6O)_{in}} \times 100 \quad (5)$$

$$H_2\ yield(\%) = \frac{n(H_2)_{out}}{6[n(C_2H_6O)_{in}]} \times 100 \quad (6)$$

where $n(C_2H_6O)_{in}$, $n(C_2H_6O)_{out}$ and $n(H_2)_{out}$ are the flow rates (mol·s^{-1}) of C_2H_6O and H_2 at the reactor inlet and outlet, respectively.

3. Results and discussion

3.1. Feedstock evaluation

The feedstock powders were evaluated using FE-SEM images, as it is reported that zirconia-based powders tend to undergo agglomeration using the laser diffraction particle size analysis [55–57]. Fig. 2a–b shows the quasi-spherical morphology of YDZ particles and the histogram plot of the particle size distribution for YDZ. The average particle size for the YDZ powder was 30 ± 1 μm, while the d_{50} and d_{90} parameters were 27 μm and 47 μm, respectively. Fig. 2c illustrates the Cobalt(II) acetate tetrahydrate powder, evidencing its morphology consisting of cubical and angular particles. The FE-SEM sample preparation involved random placement of these particles on a stand, leading to particle size measurements in a single direction for all powders. As a result, the particle

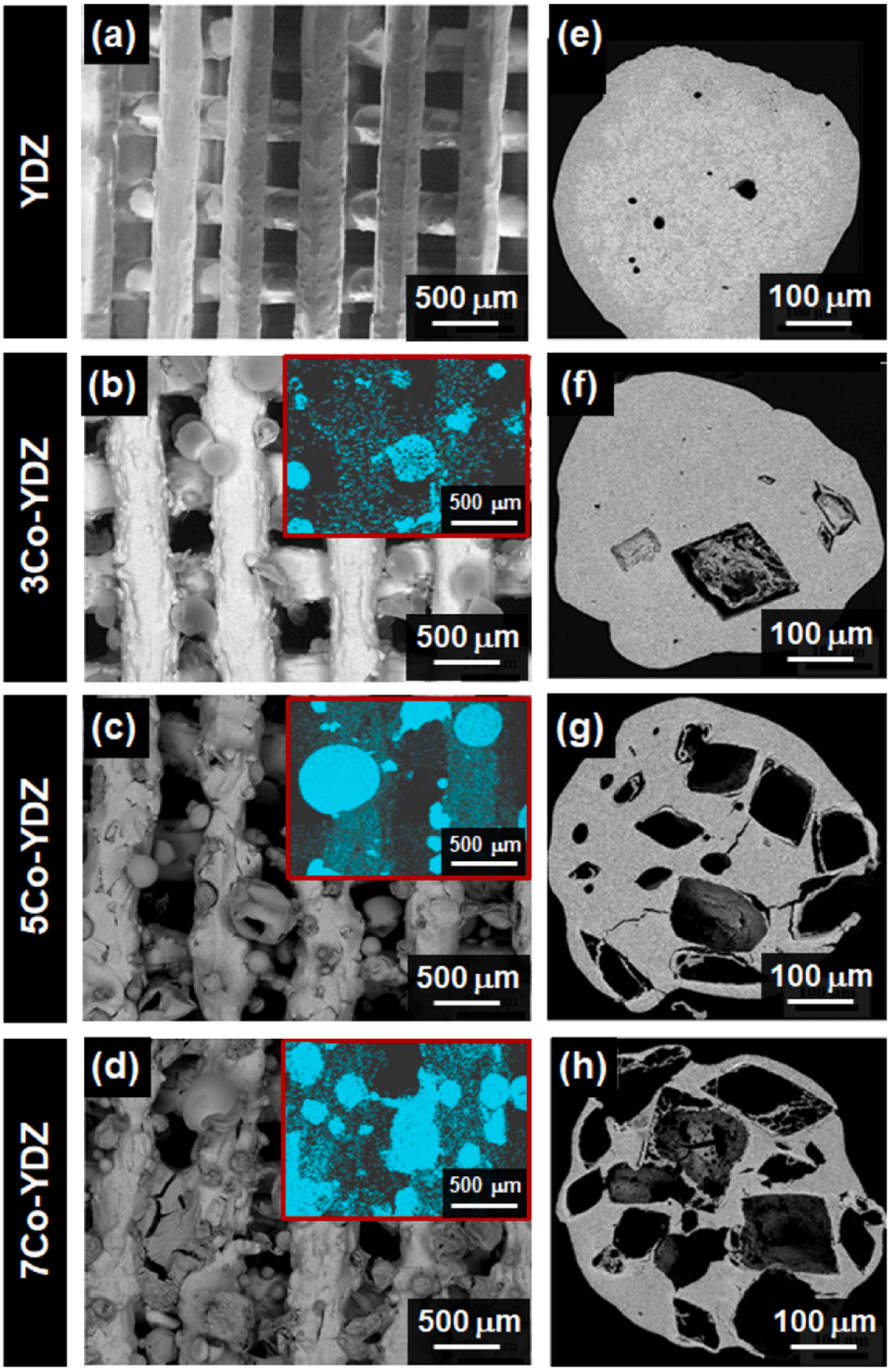

Fig 6. (a–d) Surface FE-SEM images corresponding to the microstructures of one layer for each monolith after sintering. The inset images in (b–d) show the EDS mappings of Co. (e–h) Cross-sectional FE-SEM images of the filaments for each monolith.

size for this powder was determined randomly. The average particle size for cobalt acetate tetrahydrate powder was 154 ± 23 µm. Additionally, the d_{50} and d_{90} parameters were 159 µm and 246 µm, respectively.

3.2. Rheological properties of the inks

The rheological properties are essential to evaluate the printability of monoliths with complex shapes using the DIW technology. A ceramic ink for DIW should show proper flowability during the extrusion and fast recovery to a solid state after printing. Therefore, studying the rheological properties of the inks is critical before printing. Fig. 3a shows the viscosity as a function of the shear rate for the flow sweep test represented in a logarithmic scale. For all developed inks, the viscosity decreased by increasing the shear rate, which evidences that the shear-thinning behaviour for all the inks overcame the first requirement of the DIW process [53],[58]. Although the viscosity at low shear rate is enhanced by increasing the Co content of the inks, the ink of 7Co-YDZ has a lower viscosity compared with the 3Co-YDZ and 5Co-YDZ inks above 100 s^{-1}. Due to the close proximity and multiple intersections of these lines, the flow consistency parameter (k) and flow behaviour index (n) in the Ostwald-de Waele power law can be used to compare the flow behaviour of inks, as depicted in Fig. 3b. The (n) parameter for all examined inks was less than 0.4, showing the shear-thinning behaviour for all the inks. By increasing the cobalt content, the flow behaviour

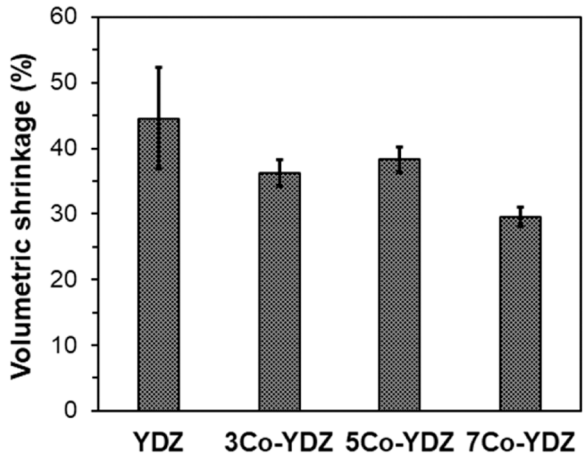

Fig. 7. The volumetric shrinkage percentage for monoliths after the sintering process.

index decreases, which corresponds to an enhanced shear-thinning behaviour in the inks with higher cobalt content. Additionally, an increase in the cobalt content results in a rise of the flow consistency parameter (k) for the cobalt-containing inks. Given the direct relationship between the parameter (k) and viscosity, it can be inferred that adding more cobalt acetate to the ink leads to an increase in viscosity.

The results of the amplitude sweep test depicted in Fig. 4a show the effect of the ink composition on the storage modulus (G′) and loss modulus (G") at different oscillation stresses. At low oscillation stresses, both G' and G'' present a constant value, showing a linear viscoelastic (LVE) behaviour. In this way, as the value of G' is higher than G'', the inks behave the same as a solid material. As the stress increased, a solid-to-liquid transformation occurred after crossing the G' and G" curves at the flow point. The storage modulus for all the inks in the LVE region is more than 10^5 Pa. Zhang et al. [56] considered that G' values of 10^5-10^6 Pa as an acceptable range for a printable ink. Therefore, the ink printability is kept by adding the Co precursor up to 30 wt%. Fig. 4b exhibits the change of the yield stress for the different inks. Although it is clear that yield stress is decreased by increasing the cobalt content in the inks, the values obtained for all inks were enough for the printability of all monoliths, because the printed filaments could tolerate the weight of the upper layers without significant deformations, as a previous work reported [59]. Therefore, all four inks present suitable rheological characteristics, indicating their potential for successful printing. However, the ink containing 7 wt% Co may exhibit a limitation in self-standing capability after printing, due to its yield stress being lower than for the other inks, potentially resulting in reduced structural integrity for large size prints. The viscoelastic properties revealed in the amplitude sweep test enable nearly complete recovery in the third phase of the 3-ITT test [53], as shown in Fig. 4c. It is evident that by increasing the shear strain within the range of 120–180 s, the value of G" surpasses that of G′, which shows the liquid behavior in the inks. In the third step, all inks exhibit good recovery ability. The YDZ, 3Co-YDZ, 5Co-YDZ, and 7Co-YDZ inks present 31 %, 30 %, 37 %, and 45 % recovery in the storage modulus (G′), respectively. These findings indicate that the inks rapidly regain their solid-like properties, which helps to keep the shape of the nozzle in the printed filaments. Consequently, all inks exhibit enough printability for using the DIW 3D printing method. Thus, these inks have the required properties to fabricate self-supporting 3D structures with enough shape accuracy, similar to the monoliths with the considered dimensions.

3.3. Debinding and sintering processes of the monoliths

After the successful printing of monoliths by the DIW process, a one-step thermal treatment was performed on green monoliths that includes: (1) precursor decomposition, (2) organic debinding, and (3) ceramic sintering. The thermal treatment was carried out under air atmosphere, as the debinding process and the gelling agent's burning occur at around 200ºC [48]. In contrast, such temperature is shifted to 350–370ºC under the N_2 atmosphere. According to previous works [48–50], the thermal decomposition processes under air atmosphere take place in the following three steps: (1) the precursor dehydration and evaporation of water between room temperature and 150ºC; (2) the degradation of the Pluronic® F-127 and the debinding of the polymeric agent present in the ceramic feedstock in the temperature range of 170–200ºC, and (3) the complete decomposition of cobalt acetate tetrahydrate from ~200 to ~300ºC forming Co_3O_4 particles. Additionally, it is important to note that the Co_3O_4 particles reach a minimum size at the temperature range of 500–700ºC. However, sintering at about 300ºC or higher than 700ºC significantly increases the particle size. The present work designed the

Table 2
Surface composition (wt%) obtained by XPS for the monoliths: 3Co-YDZ, 5Co-YDZ, and 7Co-YDZ.

Sample	Co at the ink	Co	Y	Zr	O
3Co-YDZ	3.0	4.6	9.3	66.5	19.6
5Co-YDZ	5.0	6.5	8.4	64.9	20.2
7Co-YDZ	7.0	9.3	7.9	62.9	19.9

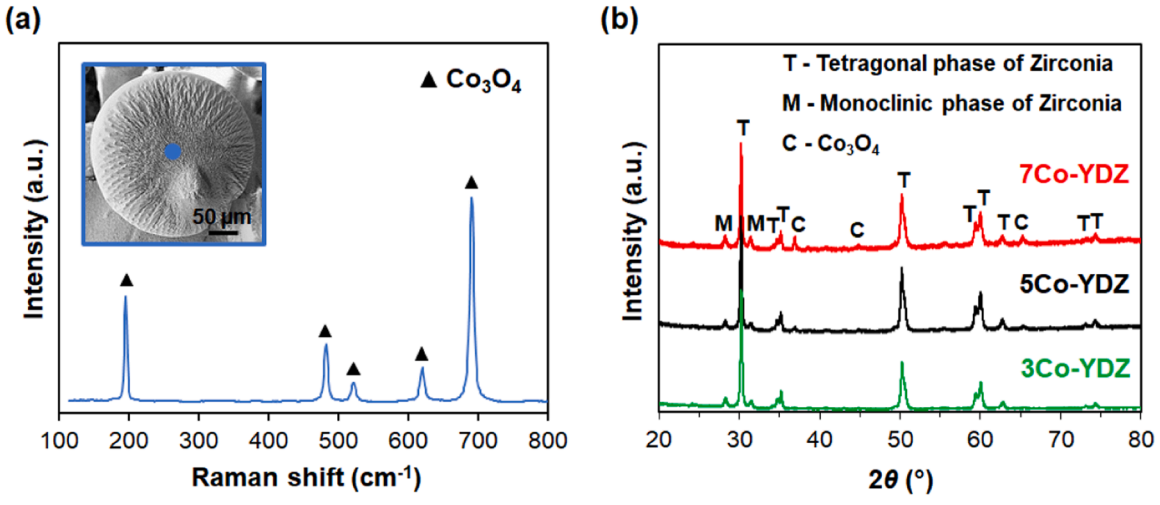

Fig. 8. (a) Raman spectra for particles at the surface of monoliths. (b) X-ray diffraction (XRD) patterns of 3Co-YDZ, 5Co-YDZ, and 7Co-YDZ samples.

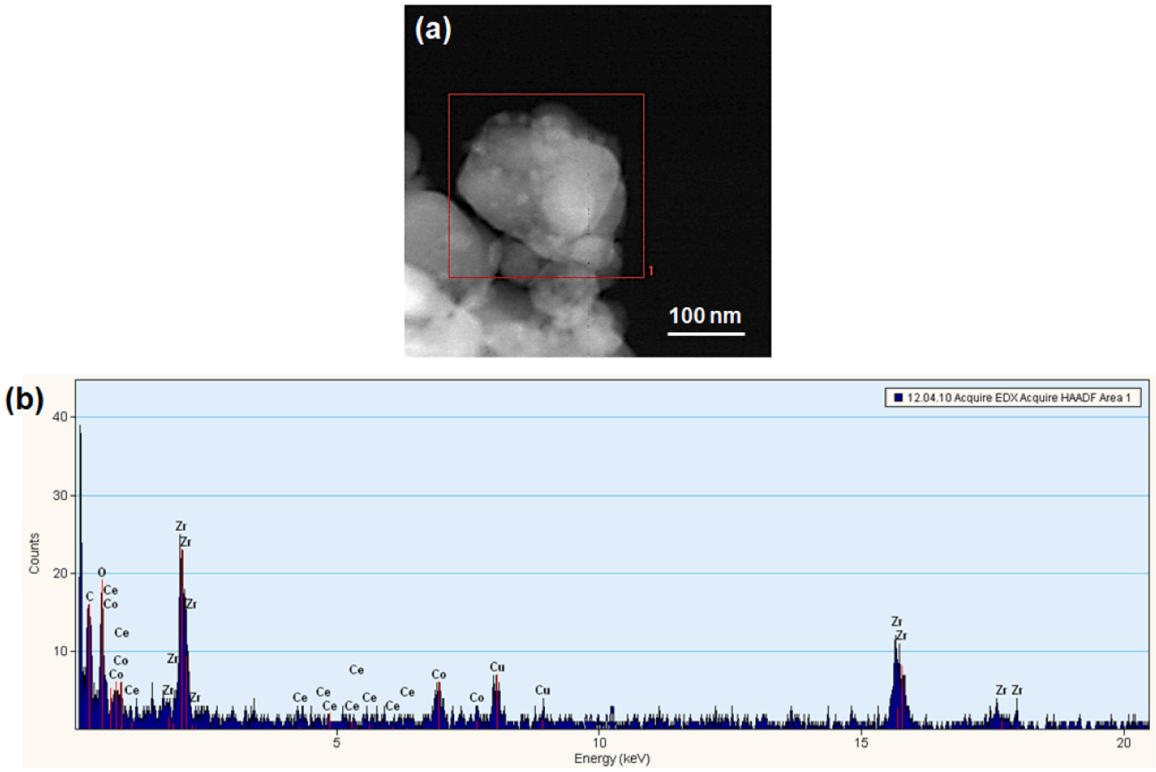

Fig. 9. (a) STEM image and (b) EDS spectra of several precursor particles corresponding to the 5Co-YDZ sample after the sintering process.

thermal treatment with a heating rate of 1.5°C·min^{-1} to achieve gradual decomposition and transformation processes (Fig. 5a). Each step is consolidated by using temperature plateaus at 200ºC for 1 h, 450ºC for 1 h, and 600ºC for 2 h, where the dwelling times were distributed according to the established organic burn out and transformation processes. The cooling rate was performed at 1.5°C·min^{-1}. Fig. 5b–e show the appearance of the four monoliths, which were fabricated with different amounts of Co precursor, after the sintering process at 600°C. It is observed that adding cobalt(II) acetate tetrahydrate to the ink results in a remarkable color change in the filaments after sintering, which is attributed to the transformation from cobalt acetate tetrahydrate to Co_3O_4 [49,60]. Furthermore, large particles appear on the surface of filaments. The amount of these particles and the dark color of filaments are increased with the Co precursor content.

3.4. Catalyst characterization

Fig. 6a–d show the FE-SEM images obtained with the BSE detector of the filament surfaces for the different monoliths. The diameter of the filaments and the separation between contiguous filaments are increased with the Co precursor content. Fig. 6e–h exhibits the macro-porosity within the cross-section structure of the monolith's filaments, confirming that the dimensional differences of the filaments are attributed to the formation of macro-porosity at the inside of the filaments during sintering at 600°C. In addition, the effect of a differential shrinkage between monoliths is discarded, as the shrinkage values of YDZ, 3Co-YDZ and 5Co-YDZ monoliths after sintering are nearly identical (Fig. 7), and only the 7Co-YDZ monolith is about 10 % less than for the other monoliths. To incorporate the precursor with 7.0 wt% Co into the final structure, as shown in Table 1, more than 40 wt% of the solid loading of cobalt acetate tetrahydrate is required as a Co precursor. After sintering these components at 600°C, the Co precursor is decomposed, which results in the loss of about 70 wt% [49,61]. The released components form a large amount of pores from entrapped gas, thus strongly affecting the porosity of the material. In this regard, these closed macro-pores limit the shrinkage of the structure during sintering.

On the other hand, the presence of semispherical macro-particles on the filaments is also observed in Fig. 6a–d, which present a diameter from 50 to 200 μm and an aspect darker than the filament surfaces. The concentration and size of these macro-particles increase with the cobalt content in the ink formulations. Therefore, it suggests that these macro-particles present a composition different to the surface of filaments, which could form cobalt oxides. As shown in Fig. 6i–k, the EDS mappings of Co corresponding to the microstructures of one layer for each monolith exhibit a high Co concentration in the macro-particles and filaments. The presence of Co cation was also detected on the entire surface of the filaments, particularly for 5Co-YDZ and 7Co-YDZ. Furthermore, increasing the percentage of cobalt up to 7 wt% Co in monoliths increases not only the concentration and volume of these macro-particles, but also the Co concentration on the surface of the filaments.

To determine the phase present in these macro-particles, Raman spectroscopy was carried out. As shown in Fig. 8a, the Raman spectra of these particles revealing Raman bands corresponding to spinel Co_3O_4 phase [62,63]. According to a previous work [60], the CoO with a faced-centered cubic structure is transformed to spinel Co_3O_4 phase in the temperature range of 200–600ºC under air atmosphere, which completely matches the thermal treatment of the monoliths in the present study. In addition to the Raman analysis, Fig. 8b displays the XRD patterns of the 3Co-YDZ, 5Co-YDZ, and 7Co-YDZ samples, highlighting the phase composition of the sintered monoliths. The XRD pattern of the 3Co-YDZ sample mainly presents the tetragonal phase of zirconia with low monoclinic content and low cobalt incorporation. As the concentration of cobalt precursor in the ink increases, the intensity of peaks associated with Co_3O_4 in the monoliths also rises compared to the 3Co-YDZ monolith. In the 7Co-YDZ sample, there is a further significant increase in the intensity of cobalt oxide peaks. These results confirm the successful incorporation of cobalt into the YDZ structure and demonstrate a clear correlation between higher cobalt content in the ink and the presence of cobalt oxide phases at the surface of filaments.

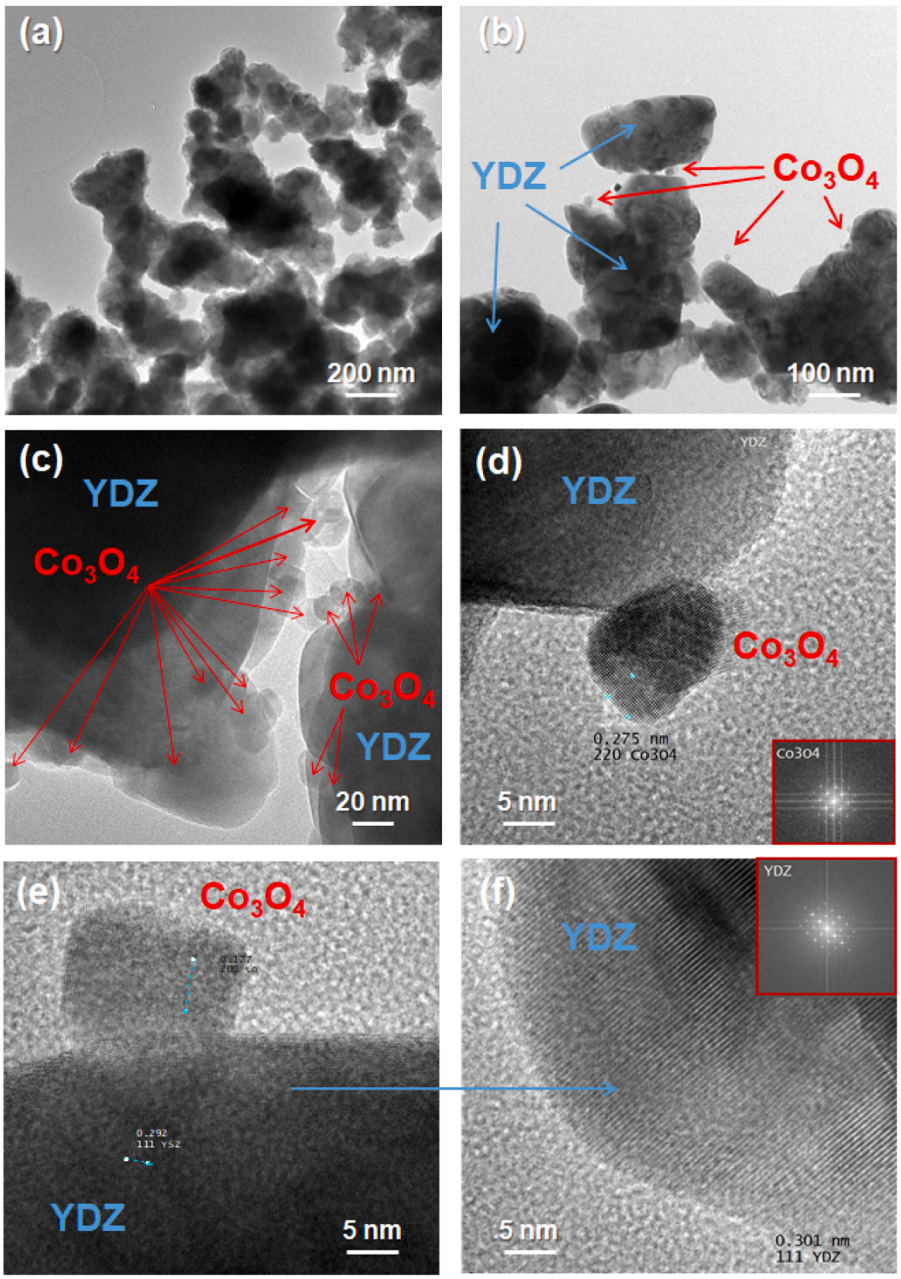

Fig. 10. HR-TEM images of: (a) general view, and (b–c) magnified views of the precursor particles corresponding to the 5Co-YDZ monolith. (c) Detailed view showing several YDZ particles covered by multiple Co_3O_4 nanoparticles, and (d–f) enhanced view of Co_3O_4 nanoparticles supported on the YDZ particles. The inset images in (d) and (f) show the Selected Area Electron Diffraction (SAED) of Co_3O_4 and YDZ, respectively.

The percentage (wt%) of each sample near the surface has been determined through XPS analysis. XPS results are summarized in Table 2, where the surface composition of different elements for the monoliths with Co is reported. The samples present a Co content (in wt %) of 4.6, 6.5, and 9.3 for 3Co-YDZ, 5Co-YDZ, and 7Co-YDZ, respectively. Thus, a significant increase of Co content with respect to their theoretical values at the ink is observed, which is in accordance with the SEM-EDS analyses. These results confirm that the surface Co amount after sintering become higher than that of the ink composition, evidencing that the Co cations segregate on the surface due to the Co diffusion during the sintering process. Thus, it suggests that this method of metal incorporation may be considered an effective strategy for fabricating monoliths with remarkably cobalt-concentrated surfaces.

Finally, the morphology, local chemical and structural analysis of the catalyst layer were carried out using STEM-EDS and HR-TEM. Fig. 9 shows STEM images and the EDS spectra of the particles corresponding to the 5Co-YDZ sample. Larger particles of YDZ and smaller particles of cobalt oxide in close contact with YDZ are observed. As shown in Fig. 10, HR-TEM images confirm that the cobalt oxide particles supported on YDZ particles between 100 and 200 nm were in the range of 5–15 nm, as is the case for the particles in Fig. 10b,c. These nanoparticles nucleate on the surface of the YDZ, more preferably in the bulk, since at the edges of cobalt was acquired by EDS. In Fig. 10c,d,e, HR-TEM images shows interplanar distances of 0.255 nm and 0.308 nm attributed to (311) Co_3O_4 and (111) YDZ, respectively. In another region (Fig. 10c,f), the Co/YDZ exhibits interplanar distances of 0.177 nm and 0.275 nm, which corresponds to (200) and (220) Co_3O_4, respectively; and 0.292 nm and 0.301 nm, which corresponds to (111) YDZ. Thus, these analyses confirm that the catalyst is formed by well-dispersed Co_3O_4 nanoparticles supported on the surface of YDZ particles.

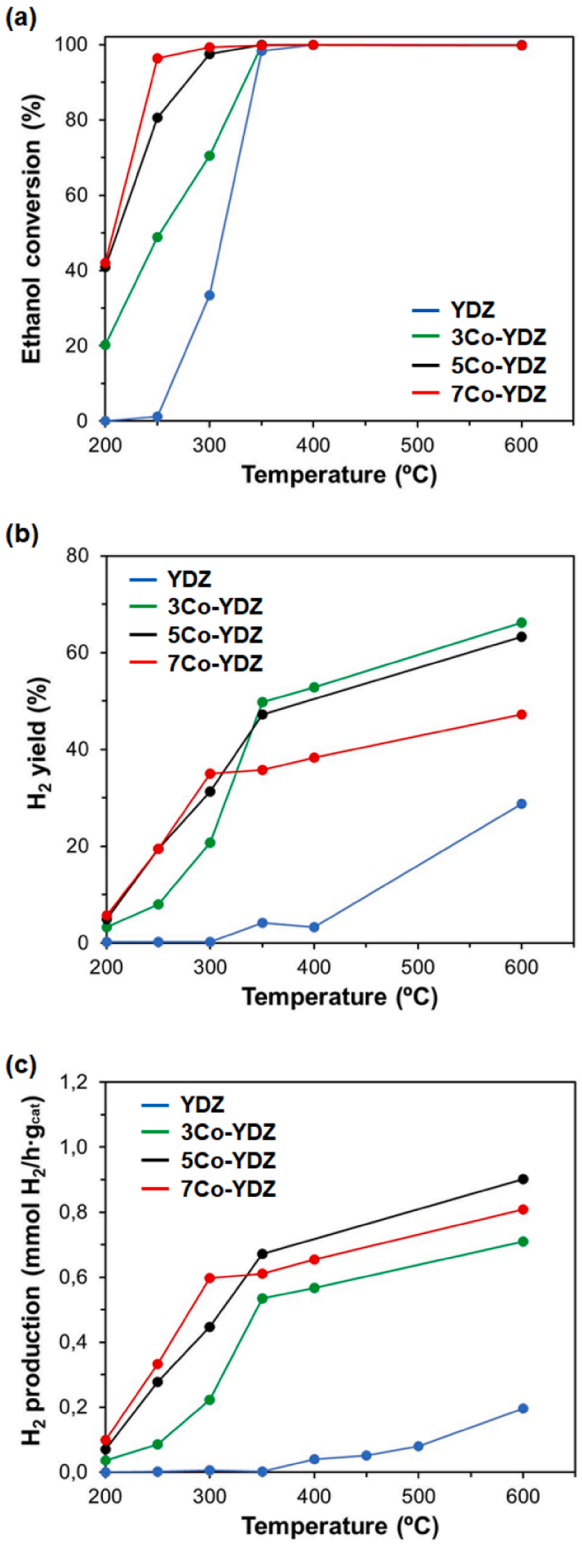

Fig. 11. (a) Ethanol conversion, (b) H_2 yield, and (c) H_2 production rate as a function of the reaction temperature for YDZ, 3Co-YDZ, 5Co-YDZ and 7Co-YDZ monoliths.

3.5. Catalytic assessment

Co-YDZ monoliths were tested under ethanol steam reforming conditions for hydrogen production. Fig. 11 shows the ethanol conversion, H_2 yield and the H_2 production rate (amount of H_2 produced in mmol per gram of catalyst per hour) as a function of operation temperature for Co-YDZ monoliths, which are compared with the YDZ monolith as a reference sample. The increase of the Co at the monoliths initiated and reached high values of ethanol conversion at lower temperatures compared with the YDZ monolith. The 5Co-YDZ and 7Co-YDZ monoliths reached ca. 81 % and 96 % conversion, respectively, at a temperature as low as 250°C, whereas the complete ethanol conversion of YDZ sample was reached at 350°C. In terms of H_2 yield, both 5Co-YDZ and 7Co-YDZ achieved the highest values at low temperature (250–300ºC). Above 300ºC, the H_2 yield of 5Co-YDZ was very close to 3Co-YDZ, and much higher than 7Co-YDZ. Thus, the 5Co-YDZ monolith displays the highest H_2 yield in the temperature range from 200 to 600ºC. In addition, the H_2 yield of the Co-YDZ monoliths was much higher than that of the reference YDZ sample. It shows the important impact of the Co on the H_2 yield, particularly in the temperature range of 200–400ºC. For the H_2 production rate, all samples exhibit the same tendency, i.e. the production of H_2 strongly increases with the temperature between 200ºC and 350ºC, and moderately above 350ºC. Comparing the different samples at each temperature, the generated H_2 is raised with the increase of the Co at the monolith, except for the 7Co-YDZ monolith, which presented a H_2 production lower than 5Co-YDZ from 350ºC to 600ºC. Table 3 summarizes parameters related to the catalytic reaction, such as GHSV, contact time (inverse to GHSV), ethanol conversion, and hydrogen production at the temperatures of 300, 350 and 600ºC.

Table 3
Values of GHSV, contact time (defined as the inverse of GHSV), ethanol conversion and hydrogen production of the monolithic structures.

Sample	GHSV (h^{-1})	Contact time (s)	T (ºC)	X_{EtOH} (%)	H_2 (mmol H_2/ h·g_{cat})
YDZ	614	5.9	300	33	0.01
			350	98	0.01
			600	100	0.20
3Co-YDZ	610	5.9	300	70	0.22
			350	99	0.53
			600	100	0.71
5Co-YDZ	606	5.9	300	97	0.45
			350	100	0.67
			600	100	0.90
7Co-YDZ	532	6.8	300	99	0.60
			350	100	0.61
			600	100	0.81

4. Conclusions

Co-YDZ monolithic catalysts were successfully obtained using a novel single-step fabrication process based on Direct-Ink Writing of Co-enriched ceramic inks and sintering process to carry out the ethanol steam reforming reaction. The feasibility of this novel approach was explored varying the Co precursor amount and studying its influence on the rheological properties of inks and the catalytic performance. The main conclusions were the following:

- Rectilinear monoliths were successfully printed at 50 % infill using YDZ ceramic inks with 3.0, 5.0 and 7.0 wt% Co, using cobalt(II) acetate tetrahydrate as a precursor of the metallic phase and keeping constant the solid loading at 70 wt% for all inks.
- Rheology analyses showed that all inks present suitable rheological characteristics for Direct-Ink Writing. However, the ink containing 7 wt% Co exhibited a limitation in self-standing capability after printing, due to its lowest yield stress, potentially resulting in reduced structural integrity for large size prints.

- Printed monolithic catalysts were debinded and sintered at 600ºC in a single thermal treatment under air atmosphere, which was designed to reduce the production steps and simultaneously prevent large size growth of Co_3O_4 particles during thermal treatment.
- The metallic active phase was successfully incorporated into monolith structures, obtaining strongly Co-rich surfaces according to XPS analysis. HR-TEM analysis confirms that the Co_3O_4 particles supported on YDZ particles between 100 and 200 nm were in the range of 5–15 nm, which is adequate for catalysis purposes.
- The 5.0 wt% Co monolith presented the best balance between catalytic activity in the steam reforming of ethanol to produce hydrogen, printability and structural integrity, reaching the complete ethanol conversion and the highest H_2 production in the temperature range of 300 −600ºC.

This work represents an example of a significant reduction of the monolithic catalyst production steps by the implementation of Direct-Ink Writing and a single thermal treatment, which constitutes a step forward towards the fabrication of fully 3D-printed catalysts.

CRediT authorship contribution statement

Gemma Fargas: Writing – review & editing, Visualization, Validation, Supervision, Project administration, Investigation, Funding acquisition, Formal analysis, Conceptualization. **Tània Vilella:** Visualization, Validation, Software, Methodology, Investigation, Data curation. **Isabel Serrano:** Visualization, Validation, Resources, Methodology, Investigation, Formal analysis, Data curation. **Miguel Ángel Laguna-Bercero:** Writing – review & editing, Visualization, Validation, Software, Resources, Methodology, Investigation, Funding acquisition, Formal analysis, Data curation. **Jordi Llorca:** Writing – review & editing, Visualization, Validation, Supervision, Resources, Project administration, Methodology, Investigation, Funding acquisition, Conceptualization. **Miguel Morales:** Writing – review & editing, Writing – original draft, Visualization, Validation, Supervision, Software, Resources, Project administration, Methodology, Investigation, Funding acquisition, Formal analysis, Data curation, Conceptualization. **Seyed Ali Razavi:** Writing – review & editing, Writing – original draft, Validation, Software, Methodology, Investigation, Formal analysis, Data curation, Conceptualization. **Daniel Rodríguez:** Writing – review & editing, Resources, Funding acquisition. **Maria-Pau Ginebra:** Writing – review & editing, Funding acquisition. **Luis Llanes:** Writing – review & editing, Resources, Project administration, Funding acquisition, Formal analysis.

Declaration of Competing Interest

The authors declare that they have no known competing financial interests or personal relationships that could have appeared to influence the work reported in this paper.

Acknowledgements

The research reported in this paper received support from the EU Regional Development Fund through the Operational FEDER of Catalonia 2014–2020 RIS3CAT-BASE3D, from projects PID2021–124572OB-C31, PID2021–125150OB-I00, PID2021–126614OB-I00, PID2022–137274NB-C32, and PID2022–137626OB-C31 funded by MCIN/AEI/10.13039/501100011033, EU and FEDER. This work was part of Maria de Maeztu Units of Excellence Programme CEX2023–001300-M funded by MCIN/AEI/10.13039/501100011033. This research was also supported by MCIN with funding from NextGenerationEU (PRTR-C17.I1) within the Planes Complementarios con CCAA (Area of Green Hydrogen and Energy) and it has been carried out in the CSIC Interdisciplinary Thematic Platform (PTI+) Transición Energética Sostenible+ (PTI-TRANSENER+). Additional funding was also received from AGAUR (Agency for Administration of University and Research) under grant numbers 2021 SGR 01053 and 01061, and 2017 SGR 1165, and from T02–20R (DGA). S.A.R. acknowledges the Ph.D. scholarship received from Universitat Politècnica de Catalunya and Banco Santander (Predoctoral grant 2020 FPU-UPC_068). T.V. acknowledges the Ph.D. scholarship received from the Barcelona Research Center in Multiscale Science and Engineering of the UPC. M.M and J.Ll. are Serra Hunter Fellows and J.Ll. and M.P.G. are grateful to ICREA Academia Program (Generalitat de Catalunya). Furthermore, the use of Servicio General de Apoyo a la Investigación (SAI, University of Zaragoza) and the Advanced Microscopy Laboratory (LMA) are also acknowledged. The authors also thank Oscar Escuer and Marc Torrente for their assistance during this research.

References

[1] T.A. Nijhuis, A.E.W. Beers, T. Vergunst, I. Hoek, F. Kapteijn, J.A. Moulijn, Preparation of monolithic catalysts, Catal. Rev. 43 (2001) 345–380, https://doi.org/10.1081/CR-120001807.
[2] F. Kapteijn, J.A. Moulijn, Structured catalysts and reactors – perspectives for demanding applications, Catal. Today 383 (2022) 5–14, https://doi.org/10.1016/J.CATTOD.2020.09.026.
[3] K. Huang, L. Wang, S. Lin, Y. Xu, D. Wu, Comparison of random and monolithic fixed-bed reactors for the oxidative dehydrogenation of butene to butadiene, J. Taiwan Inst. Chem. Eng. 63 (2016) 61–70, https://doi.org/10.1016/J.JTICE.2016.03.023.
[4] H.M. Park, A multiscale modeling of fixed bed catalytic reactors, Int. J. Heat. Mass Transf. 116 (2018) 520–531, https://doi.org/10.1016/J.IJHEATMASSTRANSFER.2017.09.035.
[5] W. Guo, W. Xiao, M. Luo, Comparison among monolithic and randomly packed reactors for the methanol-to-propylene process, Chem. Eng. J. (2012) 207–208, https://doi.org/10.1016/J.CEJ.2012.07.046, 734–745.
[6] M.Z. Granlund, O. Görke, P. Pfeifer, L.J. Pettersson, Comparison between a micro reactor with multiple air inlets and a monolith reactor for oxidative steam reforming of diesel, Int. J. Hydrog. Energy 39 (2014) 18037–18045, https://doi.org/10.1016/J.IJHYDENE.2014.06.096.
[7] O. Sanz, I. Velasco, I. Reyero, I. Legorburu, G. Arzamendi, L.M. Gandía, M. Montes, Effect of the thermal conductivity of metallic monoliths on methanol steam reforming, Catal. Today 273 (2016) 131–139, https://doi.org/10.1016/J.CATTOD.2016.03.008.
[8] S. Govender, H.B. Friedrich, Monoliths: a review of the basics, preparation methods and their relevance to oxidation, Catalysts 7 (7) (2017) 62, https://doi.org/10.3390/CATAL7020062, 62.
[9] F.N. Aguero, B.P. Barbero, L.C. Almeida, M. Montes, L.E. Cadús, MnOx supported on metallic monoliths for the combustion of volatile organic compounds, Chem. Eng. J. 166 (2011) 218–223, https://doi.org/10.1016/J.CEJ.2010.10.064.
[10] H. Liao, P. Zuo, M. Liu, Study on the correlation between the surface active species of Pd/cordierite monolithic catalyst and its catalytic activity, Mater. Sci. Eng. B 211 (2016) 45–52, https://doi.org/10.1016/J.MSEB.2016.04.015.
[11] G. Long, M. Chen, Y. Li, J. Ding, R. Sun, Y. Zhou, X. Huang, G. Han, W. Zhao, One-pot synthesis of monolithic Mn-Ce-Zr ternary mixed oxides catalyst for the catalytic combustion of chlorobenzene, Chem. Eng. J. 360 (2019) 964–973, https://doi.org/10.1016/J.CEJ.2018.07.091.
[12] F.N. Aguero, B.P. Barbero, O. Sanz, F.J.E. Lozano, M. Montes, L.E. Cadús, Influence of the support on MnOx metallic monoliths for the combustion of volatile organic compounds, Ind. Eng. Chem. Res. 49 (2010) 1663–1668, https://doi.org/10.1021/IE901567A.
[13] L. Jiang, N. Yang, J. Zhu, C. Song, Preparation of monolithic Pt–Pd bimetallic catalyst and its performance in catalytic combustion of benzene series, Catal. Today 216 (2013) 71–75, https://doi.org/10.1016/J.CATTOD.2013.05.026.
[14] Y. Hakat, T.V. Kotbagi, M.G. Bakker, Silver supported on hierarchically porous SiO2 and Co3O4 monoliths: efficient heterogeneous catalyst for oxidation of cyclohexene, J. Mol. Catal. A Chem. 411 (2016) 61–71, https://doi.org/10.1016/J.MOLCATA.2015.10.015.
[15] Z. Wang, K. Zhao, B. Xiao, P. Gao, D. He, T. Cai, J. Yuan, Fabrication of monolithic catalysts: comparison of the traditional and the novel green methods, Catalysts 9 (9) (2019) 981, https://doi.org/10.3390/CATAL9120981, 981.
[16] J. Kim, R. Kumar, A.J. Bandodkar, J. Wang, Advanced materials for printed wearable electrochemical devices: a review, Adv. Electron. Mater. 3 (2017) 1600260, https://doi.org/10.1002/AELM.201600260.
[17] S. Tagliaferri, A. Panagiotopoulos, C. Mattevi, Direct ink writing of energy materials, Mater. Adv. 2 (2021) 540–563, https://doi.org/10.1039/D0MA00753F.
[18] A. Tarancón, V. Esposito, M. Torrell, M. Di Vece, J.S. Son, P. Norby, S. Barg, P. S. Grant, A. Vogelpoth, S. Linnenbrink, M. Brucki, T. Schopphoven, A. Gasser, E. Persembe, D. Koufou, S. Kuhn, R. Ameloot, X. Hou, K. Engelbrecht, C.R.H. Bahl, N. Pryds, J. Wang, C. Tsouris, E. Miramontes, L. Love, C. Lai, X. Sun, M.R. Kærn, G. Criscuolo, D.B. Pedersen, roadmap on 3D printing for energy, J. Phys. Energy 4 (2022) (2022) 011501, https://doi.org/10.1088/2515-7655/AC483D.
[19] T. Lube, M. Staudacher, A.K. Hofer, J. Schlacher, R. Bermejo, Stereolithographic 3D printing of ceramics: challenges and opportunities for structural integrity, Adv. Eng. Mater. 25 (2023) 2200520, https://doi.org/10.1002/ADEM.202200520.

[20] J.C. Ruiz-Morales, A. Tarancón, J. Canales-Vázquez, J. Méndez-Ramos, L. Hernández-Afonso, P. Acosta-Mora, J.R. Marín Rueda, R. Fernández-González, Three dimensional printing of components and functional devices for energy and environmental applications, Energy Environ. Sci. 10 (2017) 846–859, https://doi.org/10.1039/C6EE03526D.

[21] S. Hajimirzaee, A.M. Doyle, 3D printed catalytic converters with enhanced activity for low-temperature methane oxidation in dual-fuel engines, Fuel 274 (2020) 117848, https://doi.org/10.1016/J.FUEL.2020.117848.

[22] J. Schlacher, T. Lube, W. Harrer, G. Mitteramskogler, M. Schwentenwein, R. Danzer, R. Bermejo, Strength of additive manufactured alumina, J. Eur. Ceram. Soc. 40 (2020) 4737–4745, https://doi.org/10.1016/J.JEURCERAMSOC.2020.03.073.

[23] O.H. Laguna, P.F. Lietor, F.J.I. Godino, F.A. Corpas-Iglesias, A review on additive manufacturing and materials for catalytic applications: milestones, key concepts, advances and perspectives, Mater. Des. 208 (2021) 109927, https://doi.org/10.1016/J.MATDES.2021.109927.

[24] K. Fu, Y. Su, Y. Zheng, R. Han, Q. Liu, Novel monolithic catalysts for VOCs removal: a review on preparation, carrier and energy supply, Chemosphere 308 (2022) 136256, https://doi.org/10.1016/J.CHEMOSPHERE.2022.136256.

[25] S.A. Razavi, G. Fargas, I. Serrano, M.Á. Laguna-Bercero, L. Llanes, J. Llorca, M. Morales, Cobalt-zirconia coated monoliths fabricated by direct ink writing for catalytic applications, J. Eur. Ceram. Soc. 45 (2025) 117063, https://doi.org/10.1016/J.JEURCERAMSOC.2024.117063.

[26] M.N. Tsampas, F.M. Sapountzi, P. Vernoux, Applications of yttria stabilized zirconia (YSZ) in catalysis, Catal. Sci. Technol. 5 (2015) 4884–4900, https://doi.org/10.1039/C5CY00739A.

[27] D. Theleritis, S. Souentie, A. Siokou, A. Katsaounis, C.G. Vayenas, Hydrogenation of CO 2 over Ru/YSZ electropromoted catalysts, ACS Catal. 2 (2012) 770–780, https://doi.org/10.1021/CS300072A/ASSET/IMAGES/LARGE/CS-2012-00072A_0005.JPEG.

[28] M. Morales, M. Rezayat, S. García-González, A. Mateo, E. Jiménez-Piqué, Ru-Ce0.7Zr0.3O2−δ as an anode catalyst for the internal reforming of dimethyl ether in solid oxide fuel cells, Nanomaterials 14 (14) (2024) 603, https://doi.org/10.3390/NANO14070603, 603.

[29] R.J. Isaifan, E.A. Baranova, Effect of ionically conductive supports on the catalytic activity of platinum and ruthenium nanoparticles for ethylene complete oxidation, Catal. Today 241 (2015) 107–113, https://doi.org/10.1016/J.CATTOD.2014.03.061.

[30] H.A.E. Dole, R.J. Isaifan, F.M. Sapountzi, L. Lizarraga, D. Aubert, A. Princivalle, P. Vernoux, E.A. Baranova, Low temperature toluene oxidation over Pt nanoparticles supported on yttria stabilized-zirconia, Catal. Lett. 143 (2013) 996–1002, https://doi.org/10.1007/S10562-013-1071-X/METRICS.

[31] R.J. Isaifan, H.A.E. Dole, E. Obeid, L. Lizarraga, P. Vernoux, E.A. Baranova, Metal-support interaction of Pt nanoparticles with ionically and non-ionically conductive supports for CO oxidation, Electrochem. Solid-State Lett. 15 (2012), https://doi.org/10.1149/2.024203ESL/XML.

[32] H.A. Dole, J.M. Kim, L. Lizarraga, P. Vernoux, E.A. Baranova, Catalytic CO oxidation over Au nanoparticles supported on Yttria-stabilized zirconia, ECS Trans. 45 (2012) 265–274, https://doi.org/10.1149/1.3701316/XML.

[33] H. Rönkkönen, P. Simell, M. Reinikainen, O. Krause, The effect of sulfur on ZrO2-based biomass gasification gas clean-up catalysts, Top. Catal. 52 (2009) 1070–1078, https://doi.org/10.1007/S11244-009-9255-8/METRICS.

[34] H. Rönkkönen, P. Simell, M. Niemelä, O. Krause, Precious metal catalysts in the clean-up of biomass gasification gas part 2: performance and sulfur tolerance of rhodium based catalysts, Fuel Process. Technol. 92 (2011) 1881–1889, https://doi.org/10.1016/J.FUPROC.2011.05.004.

[35] E. Obeid, L. Lizarraga, M.N. Tsampas, A. Cordier, A. Boréave, M.C. Steil, G. Blanchard, K. Pajot, P. Vernoux, Continuously regenerating diesel particulate filters based on ionically conducting ceramics, J. Catal. 309 (2014) 87–96, https://doi.org/10.1016/J.JCAT.2013.09.004.

[36] W.Y. Hernández, A. Hadjar, M. Klotz, J. Leloup, A. Princivalle, C. Tardivat, C. Guizard, P. Vernoux, NOx storage capacity of yttria-stabilized zirconia-based catalysts, Appl. Catal. B Environ. (2013) 130–131, https://doi.org/10.1016/J.APCATB.2012.09.048.

[37] W.Y. Hernandez, A. Hadjar, A. Giroir-Fendler, P. Andy, A. Princivalle, M. Klotz, A. Marouf, C. Guizard, C. Tardivat, C. Viazzi, P. Vernoux, Electrochemically-assisted NOx storage–reduction catalysts, Catal. Today 241 (2015) 143–150, https://doi.org/10.1016/J.CATTOD.2014.03.076.

[38] N. Mahato, A. Banerjee, A. Gupta, S. Omar, K. Balani, Progress in material selection for solid oxide fuel cell technology: a review, Prog. Mater. Sci. 72 (2015) 141–337, https://doi.org/10.1016/J.PMATSCI.2015.01.001.

[39] L. Bernadet, M. Morales, X.G. Capdevila, F. Ramos, M.C. Monterde, J.A. Calero, A. Morata, M. Torrell, A. Tarancón, Reversible fuel electrode supported solid oxide cells fabricated by aqueous multilayered tape casting, J. Phys Energy 3 (2021), https://doi.org/10.1088/2515-7655/ABD296.

[40] J. Llorca, N. Homs, J. Sales, P. Rańirez de la Piscina, Efficient production of hydrogen over supported cobalt catalysts from ethanol steam reforming, J. Catal. 209 (2002) 306–317, https://doi.org/10.1006/JCAT.2002.3643.

[41] M.S. Batista, R.K.S. Santos, E.M. Assaf, J.M. Assaf, E.A. Ticianelli, Characterization of the activity and stability of supported cobalt catalysts for the steam reforming of ethanol, J. Power Sources 124 (2003) 99–103, https://doi.org/10.1016/S0378-7753(03)00599-8.

[42] A. Casanovas, C. de Leitenburg, A. Trovarelli, J. Llorca, Catalytic monoliths for ethanol steam reforming, Catal. Today 138 (2008) 187–192, https://doi.org/10.1016/J.CATTOD.2008.05.028.

[43] J.F. Da Costa-Serra, A. Chica, Bioethanol steam reforming on Co/ITQ-18 catalyst: effect of the crystalline structure of the delaminated zeolite ITQ-18, Int. J. Hydrog. Energy 36 (2011) 3862–3869, https://doi.org/10.1016/J.IJHYDENE.2010.12.094.

[44] M. Morales, M. Segarra, Steam reforming and oxidative steam reforming of ethanol over La0. 6Sr0. 4CoO3− δ perovskite as catalyst precursor for hydrogen production, Appl. Catal. A Gen. 502 (2015), https://doi.org/10.1016/j.apcata.2015.05.036.

[45] C. Gaudillere, J.J. González, A. Chica, J.M. Serra, YSZ monoliths promoted with Co as catalysts for the production of H2 by steam reforming of ethanol, Appl. Catal. A Gen. 538 (2017) 165–173, https://doi.org/10.1016/J.APCATA.2017.03.008.

[46] M. Morales, M.Á. Laguna-Bercero, E. Jiménez-Piqué, Hydrogen-rich gas production by steam reforming and oxidative steam reforming of methanol over La0.6Sr0.4CoO3−δ: effects of preparation, operation conditions, and redox cycles, ACS Appl. Energy Mater. 6 (2023) 7887–7898, https://doi.org/10.1021/ACSAEM.3C00778/ASSET/IMAGES/LARGE/AE3C00778_0011.JPEG.

[47] E. Gioffredi, M. Boffito, S. Calzone, S.M. Giannitelli, A. Rainer, M. Trombetta, P. Mozetic, V. Chiono, Pluronic F127 hydrogel characterization and biofabrication in cellularized constructs for tissue engineering applications, Procedia CIRP 49 (2015) 125–132, https://doi.org/10.1016/J.PROCIR.2015.11.001.

[48] F. Álvarez, A. Cifuentes, I. Serrano, L. Franco, G. Fargas, F. Fenollosa, R. Uceda, L. Llanes, C. Tardivat, J. Llorca, J.J. Roa, Optimization of the sintering thermal treatment and the ceramic ink used in direct ink writing of α-Al2O3: characterization and catalytic application, J. Eur. Ceram. Soc. 42 (2022) 2921–2930, https://doi.org/10.1016/J.JEURCERAMSOC.2022.01.032.

[49] T. Wanjun, C. Donghua, Mechanism of thermal decomposition of cobalt acetate tetrahydrate, Chem. Pap. 61 (2007) 329–332, https://doi.org/10.2478/S11696-007-0042-3/METRICS.

[50] K. Sinkó, G. Szabó, M. Zrínyi, Liquid-phase synthesis of cobalt oxide nanoparticles, J. Nanosci. Nanotechnol. 11 (2011) 4127–4135, https://doi.org/10.1166/JNN.2011.3875.

[51] ISO13322-1:2014 - Particle Size Analysis — Image Analysis Methods — Part 1: Static Image Analysis Methods, (n.d.). ⟨https://www.iso.org/standard/51257.html⟩, (accessed August 12, 2024).

[52] A. Mazzoli, O. Favoni, Particle size, size distribution and morphological evaluation of airborne dust particles of diverse woods by scanning electron microscopy and image processing program, Powder Technol. 225 (2012) 65–71, https://doi.org/10.1016/J.POWTEC.2012.03.033.

[53] L. del-Mazo-Barbara, M.P. Ginebra, Rheological characterisation of ceramic inks for 3D direct ink writing: a review, J. Eur. Ceram. Soc. 41 (2021) 18–33, https://doi.org/10.1016/J.JEURCERAMSOC.2021.08.031.

[54] L. del-Mazo-Barbara, L. Johansson, F. Tampieri, M.P. Ginebra, Toughening 3D printed biomimetic hydroxyapatite scaffolds: polycaprolactone-based self-hardening inks, Acta Biomater. 177 (2024) 506–524, https://doi.org/10.1016/J.ACTBIO.2024.02.012.

[55] S. Roedel, J.C.M. Souza, F.S. Silva, J. Mesquita-Guimarães, M.C. Fredel, B. Henriques, Optimized route for the production of zirconia structures with controlled surface porosity for biomedical applications, Ceram. Int. 44 (2018) 12496–12503, https://doi.org/10.1016/J.CERAMINT.2018.04.042.

[56] J. Zhang, M. Yarahmadi, L. Cabezas, M. Serra, S. Elizalde, J.M. Cabrera, L. Llanes, G. Fargas, Robocasting of dense 8Y zirconia parts: rheology, printing, and mechanical properties, J. Eur. Ceram. Soc. 43 (2023) 2794–2804, https://doi.org/10.1016/J.JEURCERAMSOC.2022.11.042.

[57] M. Yarahmadi, P. Barcelona, G. Fargas, E. Xuriguera, J.J. Roa, Optimization of the ceramic ink used in direct ink writing through rheological properties characterization of zirconia-based ceramic materials, Ceram. Int. 48 (2022) 4775–4781, https://doi.org/10.1016/J.CERAMINT.2021.11.013.

[58] A. Khecho, S.A. Ghaffari, B. Eftekhari Yekta, The influence of particle size distribution on rheological properties of fused silica pastes for direct ink writing, Int. J. Appl. Ceram. Technol. 19 (2022) 2472–2479, https://doi.org/10.1111/IJAC.14109.

[59] A. M'Barki, L. Bocquet, A. Stevenson, Linking rheology and printability for dense and strong ceramics by direct ink writing, Sci. Rep 7 (2017) 1–10, https://doi.org/10.1038/s41598-017-06115-0.

[60] C.W. Tang, C.Bin Wang, S.H. Chien, Characterization of cobalt oxides studied by FT-IR, Raman, TPR and TG-MS, Thermochim. Acta 473 (2008) 68–73, https://doi.org/10.1016/J.TCA.2008.04.015.

[61] D. Gutiérrez-martín, A. Varela, J.M. González-calbet, E. Matesanz, M. Parras, Revisiting the decomposition process of Tetrahydrate Co(II) acetate: a sample's journey through temperature, Appl. Sci. 12 (2022) 6786, https://doi.org/10.3390/APP12136786/S1.

[62] V.G. Hadjiev, M.N. Iliev, I.V. Vergilov, The Raman spectra of Co3O4, J. Phys. C Solid State Phys. 21 (1988) L199, https://doi.org/10.1088/0022-3719/21/7/007.

[63] R.F.K. Gunnewiek, C.F. Mendes, R.H.G.A. Kiminami, Synthesis of spinel cobalt oxide nanoparticles using a modified polymeric precursor method, Adv. Powder Technol. 27 (2016) 1056–1061, https://doi.org/10.1016/J.APT.2016.03.013.